Multiscale Coherent Excitations in Microscopic Acoustic Wave Turbulence of Cold Dusty Plasma Liquids

Hao-Wei Hu,[1] Wen Wang,[1,2] and Lin I[1]

[1]*Department of Physics and Center for Complex Systems, National Central University, Jhongli, Taiwan 32001, Republic of China*
[2]*Molecular Science and Technology, Taiwan International Graduate Program, Academia Sinica and National Central University, Taipei, Taiwan 10617, Republic of China*

We experimentally demonstrate the observation of thermally excited microscopic acoustic wave turbulence at the discrete level in quasi-two-dimensional cold dusty plasma liquids. Through multidimensional empirical mode decomposition of individual dust particle motions over a large area, the turbulence is decomposed into multiscale traveling wave modes, sharing self-similar dynamics. All modes exhibit intermittent excitation, propagation, scattering, and annihilation of coherent waves, in the form of clusters in the xyt space, with cluster sizes exhibiting self-similar power law distribution. The poor particle interlocking in the region with poor structural order is the key origin of the easier excitations of the large amplitude slow modes. The sudden phase synchronization of slow wave modes switches particle motion from cage rattling to cooperative hopping.

Under strong external drive, wave turbulence with multiscale fluctuations ubiquitously occurs in many nonlinear *macroscopic* continuous media, such as water surface, chemical systems, nonlinear optical and acoustic media, and plasmas [1–7]. Past studies focused mainly on dispersion relations, scaling behaviors of continuous power spectra, wave mixing, multifractality, etc., [1–6], and to a lesser extent on the spatiotemporal coherent waveform behaviors at various scales [7]. In particular, to our knowledge, whether thermally excited microscopic acoustic wave turbulence (MAWT) occurs at the *discrete* atomic level also remains an unexplored fundamental issue.

Counterintuitively, coherent excitations exist in macroscopic turbulent systems under strong drives or nonlinear excitable systems driven by noise. Multiscale coherent vortices in hydrodynamic turbulence [8] and multiscale acoustic vortices with helical waveforms in macroscopic acoustic wave turbulence [7] are good examples under external persistent drives. The avalanche excitation of coherent wave clusters exhibiting power law cluster size distribution in the Belousov-Zhabotinsky reaction system is another example of a nonlinear excitable system driven by noise [9]. Microscopically, the cold, supercooled or glass-forming liquids around freezing can be viewed as nonlinearly coupled systems driven by stochastic thermal noise. Under solidlike dense packing, the competition between strong mutual coupling and weak thermal agitation causes the formation of crystalline ordered domains (CODs) with various sizes and different orientations. They have been observed in colloidal glass-forming liquids and dusty plasma liquids (DPLs) [10–17]. CODs and defects

around their interfaces can facilitate the propagation and frustration of thermally excited transverse and longitudinal acoustic waves [18,19], respectively, because CODs can temporarily sustain shears. Fourier power spectra and the instantaneous normal mode method have been used for characterizing those waves [20–25]. However, those waves have never been investigated from the wave turbulence view, especially their spatiotemporal coherence at different scales.

Acoustic waves are constituted by cooperatively moving particles. For individual particle motion, past studies mainly focused on heterogeneous non-Gaussian dynamics [11–17]. Particles alternatively exhibit small amplitude thermal rattling in cages formed by surrounding particles, and avalanchelike cooperative hopping in the form of strings or rotating CODs after accumulating sufficient constructive perturbation. The latter in turn causes structural rearrangement [11–17,26–30]. Nevertheless, how the superposition of multiscale waves leads to heterogeneous alternating rattling and hopping motions also remains unclear.

In brief, under stochastic thermal agitation, the heterogeneous microstructure affects particle mutual interaction, and consequently multiscale wave excitation and coherence. Wave superposition determines alternate particle rattling and hopping, which further affect structural and dynamical evolutions. Certainly, it is intriguing to address the following important unexplored issues in this Letter, using a cold DPL as a platform: (a) viewing these waves as MAWT in the cold liquid, (b) decomposing MAWT into multiscale traveling wave modes and characterizing their spatiotemporal coherent waveform dynamics, and
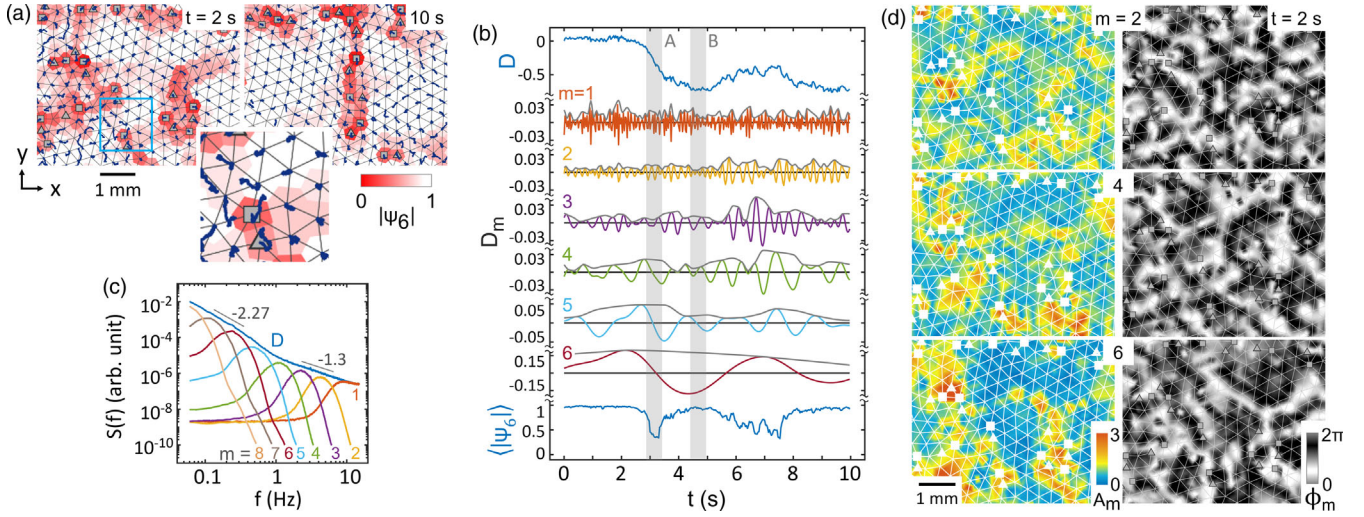
FIG. 1. (a) Two typical snapshots of particle configuration with particles sitting at the vertices of the background grid, color coded by $|\Psi_6|$, and the subsequent particle trajectories over a 4 s interval, with the inset a magnifcation of the boxed region. Squares and triangles represent sevenfold and fivefold disclination defects, respectively. (b) Temporal evolutions of relative transverse displacement D, its decomposed D_m, and $\langle|\Psi_6(t)|\rangle$ of a typical particle pair. Band A shows an example of the synchronization (for $\phi_m = 0.5\pi$) of the drastic descending parts of the larger m modes (e.g., $m > 3$), with the earlier increases of their amplitudes. It causes hopping and structural rearrangement with the large changes of D and $\langle|\Psi_6(t)|\rangle$, respectively. (c) The corresponding power spectra of D (blue line) and decomposed D_m. The numbers near the straight gray lines are their scaling exponents. (d) Particle configurations at $t = 2$ s, color coded by $A_m = a_m/\overline{a_m}$ ($m = 2, 4$, and 6) and ϕ_m, showing the heterogeneous excitations of multiscale waves.

(c) identifying correlations between different modes and local structural order, and unraveling cage rattling and hopping as the superposition of multiscale waves.

The DPL can be formed by micrometer sized particles suspended in the low pressure rf discharge [14–17,20, 21,23,24,31–35], through screened Coulomb interaction due to the strong negative charging on particles. It is a good platform for understanding the generic behaviors of the Yukawa liquid at the microscopic level directly through visualizing individual particle motions over a large area [14–17,20–24,31–37].

For turbulent-type motion with a continuous power spectrum, the absence of spectrum gaps disables spatio-temporally decomposing fluctuations into different scale modes using Fourier analysis. Here, similar to a previous study on the three-dimensional (3D) macroscopic dust acoustic wave turbulence in the *gaseous* dusty plasma [7], multidimensional complementary ensemble empirical mode decomposition (MCEEMD) is used. It enables one to decompose particle motions into spatiotemporal wave-forms at different scales with the information of instanta-neous local amplitudes, phases, and frequencies in the $(2 + 1)$D spatiotemporal space [38–41].

The experiment is conducted in a cylindrical symmetric rf dusty plasma system, as described in Refs. [15,25]. The DPL composed of short vertical chains of polystyrene particles, aligned by the vertical downward ion flow [31], is confined by the sheath field adjacent to the boundary of a hollow cylindrical trap. Particles along the same vertical chain hop together horizontally. In this quasi-2D liquid,

particle positions in the horizontal (xy) plane, illuminated by a thin horizontal laser sheet, are recorded at 30 Hz sampling rate by a CCD on top of the system.

Figure 1(a) shows two typical snapshots with particles sitting at the vertices of the background grid, color coded by the degree of local bond orientational order $|\Psi_6|$ (see its definition in Ref. [42]), and subsequent particle trajectories over a 4 s interval. Squares and triangles represent sevenfold and fivefold disclination defects, respectively. $|\Psi_6| = 1$ and <0.4 for perfect lattice sites and defect sites, respectively. Defects appear in the form of clusters around the boundaries of adjacent CODs to accommodate different lattice orientations. Regions with particles exhibiting small amplitude cage rattling (short trajectories), and collective large amplitude hopping (long trajectories) in the form of clusters [see the inset of Fig. 1(a)], can be easily identi-fied [15].

For simplicity, we focus on the transverse oscillations. The relative transverse displacement $D(t)$ of a pair of adjacent particles is used as a local dynamical variable. Here, $D(t)$ is obtained through integrating the relative velocity normal to bond direction and normalized by the mean bond length, which corresponds to bond angle evolution. The top and bottom curves of Fig. 1(b) show the $D(t)$ of a typical particle pair and $\langle|\Psi_6(t)|\rangle$, averaged over the $|\Psi_6|$ of the two particles of that pair, respectively. Between small amplitude cage rattling in both curves, hopping and the associated structural rearrangement occur (e.g., as in band A) with large variations of $D(t)$ and $\langle|\Psi_6(t)|\rangle$ over a subsecond timescale.

Through the sifting process in MCEEMD based on EMD using the Hilbert-Huang transform [7,25,38–41], $D(\mathbf{x}_i, t)$ from the local particle pair centered at point $\mathbf{x}_i$ in the xy plane is successively decomposed in terms of an adaptively obtained, amplitude-frequency modulated oscillatory intrinsic mode function (IMF) with zero mean, $D_m(\mathbf{x}_i, t)$ ($m = 1, 2, \ldots, N$), until reaching the mean trend $r(\mathbf{x}_i, t)$. Namely, $D(\mathbf{x}_i, t) = \sum_{m=1}^{N} D_m(\mathbf{x}_i, t) + r(\mathbf{x}_i, t)$ and $D_m(\mathbf{x}_i, t) = a_m(\mathbf{x}_i, t) \cos \phi_m(\mathbf{x}_i, t)$. This complete and nearly orthogonal reconstruction reveals temporal variations of the local amplitude $a_m(\mathbf{x}_i)$ and phase $\phi_m(\mathbf{x}_i)$ for $D_m(\mathbf{x}_i)$, which can be spatially extended to all particle pairs in the xy plane. More details of mode decomposition, especially through adding complementary noise sets for removing mode mixing, and the comparison of the results from several different methods based on empirical mode decomposition can be found in Refs. [25,40,41,44].

Figure 1(b) further shows the temporal evolutions of various D_m, decomposed from $D(t)$ of the top row. Figure 1(c) shows the corresponding power spectra of $D(t)$ and $D_m(t)$, averaged over the spectra of 3662 particle pairs. All of the IMFs exhibit amplitude and frequency modulations, which cause their similar spread spectra, and the

multiscale fluctuations of $D(t)$. The mode intensity increases with increasing m.

As shown in Fig. 1(b), the high frequency part of cage rattling is contributed mainly by the fast modes 1 and 2 (e.g., see the cage rattling before and after band A). The slow modes ($m > 3$) have higher amplitudes than the fast modes and play key roles in hopping. For example, before band A, their amplitudes gradually increase. The synchronization of their descending parts leads to the large drop of $D(t)$ in band A, which corresponds to the hopping region causing strong bond rotation after cage rattling. In the nonhopping region, although the amplitudes of slow modes could be larger than those of fast modes, their destructive superposition causes only a small amplitude slow variation of D (e.g., in band B).

By extending the above sifting process to all particle pairs, the spatiotemporal evolutions of all modes can be obtained. Figure 1(d) shows typical plots color coded by the instantaneous normalized local wave amplitude $A_m = a_m/\overline{a_m}$ and the instantaneous phase ϕ for different modes, at $t = 2$ s (also see Video S1 in the Supplemental Material [25] for their spatiotemporal evolution), from the same area as Fig. 1(a). Here, $\overline{a_m}$ is the averaged a_m over all particle
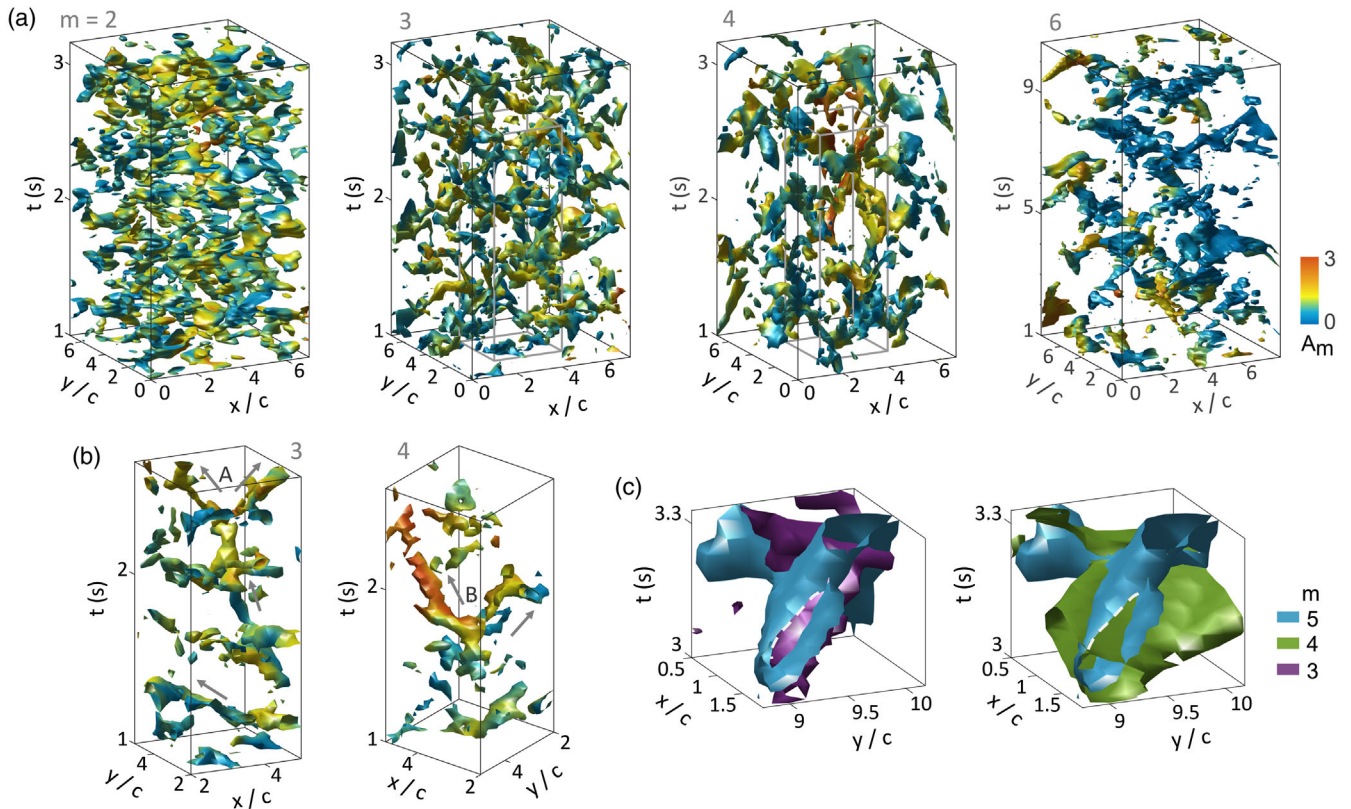

FIG. 2. (a) Isophase ($\phi_m = 0.5\pi$) surfaces, color coded by normalized amplitude A_m, of modes 2 to 6 in the xyt space. Here, c is the mean interparticle distance. (b) Isophase surface plots enlarged from cuboids in the plots with $m = 3$ and 4 of (a), more clearly showing the intermittent coherent excitation, propagation (e.g., along arrow directions), scattering, and annihilation of different mode waves, in the form of clusters. (c) Coplot of the isophase ($\phi_m = 0.5\pi$) surfaces of (left panel) modes 3 and 5, and (right panel) modes 4 and 5 in the xyt space, showing phase synchronization of modes 3 to 5 along the common intersection (white dashed line) in the xyt space.
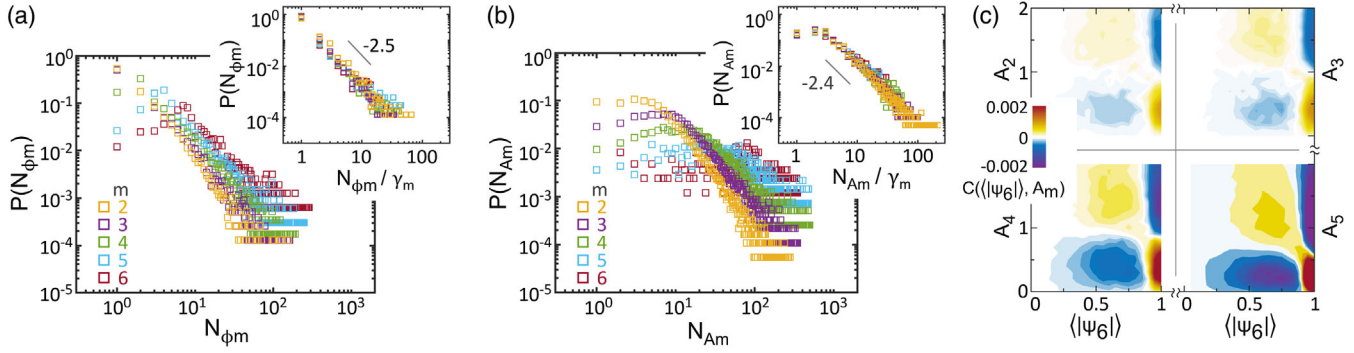
FIG. 3. (a),(b) Histograms of coherent cluster sizes, $N_{\phi m}$ and N_{Am}, the number of connected pairs of adjacent particles, sharing similar phases within the range $\phi_m = 0.5\pi \pm 0.1\pi$, and $A_m > 2$ for different modes, respectively, in the xyt space. (Insets) Corresponding histograms of cluster sizes after rescaling by γ_m, the ratio of the product of the averaged period τ_m and the square of the mean wavelength λ_m of mode m to that of mode 1, showing the collapsing of histogram curves in each set to a power law distribution. (c) Color coded plots of the correlation probability $C(\langle|\Psi_6|\rangle, A_m)$, showing the decreasing negative correlation between A_m and $|\Psi_6|$ with increasing m.

pairs and time. It demonstrates the heterogeneous excitations of different modes. The regions with large A_m (the yellow and orange regions) appear in the form of clusters with various sizes and change at different times. The corresponding instantaneous phase (ϕ_m) plots show that the white isophase regions with $\phi_m = 0.5\pi$ (i.e., $-dD_m/dt$ reaches the maximum in an oscillation cycle) appear mainly in the form of connected straight strips along the local lattice lines (see the background grids) with different orientations.

For constructing a clearer picture of the spatiotemporal evolution of the coherent waveforms at different scales, Fig. 2(a) shows the plots of the isophase surfaces with $\phi_m = 0.5\pi$ for a few typical modes, color coded by A_m in the xyt space (see more details on isophase surface construction in Ref. [45]). Note that the mode 6 plot uses different scales. Figure 2(b) shows the isophase waveforms enlarged from the cuboids of the plots for modes 3 and 4 of Fig. 2(a), with the arrows indicating wave propagating directions. Basically, those corrugated isophase surfaces are composed of tilted surfaces, with various persistent spans for sustaining the tilting angle (determined by the phase velocity of the wave) and amplitude in the xyt space. They appear in the form of clusters with various sizes in the xyt space.

Namely, the coherent wave can intermittently emerge with small local amplitude, gradually increase its spatial span and change its amplitude during propagation, alter propagation direction through scattering [e.g., at points A and B in Fig. 2(b)], and annihilate (see more details in Fig. S5 and Videos S1 and S2 in the Supplemental Material [25]). The isophase surfaces of different modes can intersect in the xyt space. The intersection (white dashed line) of isophase surfaces of the different slow modes in the example in Fig. 2(c) is the region of their phase synchronization leading to hopping with the large change of D.

The isophase surfaces and the large A_m sites of each mode both intermittently appear in the form of clusters with various sizes in the xyt space (see Video S2 in the Supplemental Material [25]). Figures 3(a) and 3(b) show the histograms of the coherent cluster size and the large A_m cluster size, i.e., the number of connected pairs, $N_{\phi m}$ and N_{Am}, sharing similar phases within the range $\phi_m = 0.5\pi \pm 0.1\pi$, and large local amplitude $A_m > 2$, respectively, for different modes in the xyt space. After rescaling $N_{\phi m}$ and N_{Am} by γ_m, the histogram curves in each set collapse to a power law distribution curve with exponents equaling -2.5 and -2.4, respectively (see the two insets of Fig. 3). Here, γ_m is the ratio of the product of the mean period and the square of the mean wavelength of mode m to that of mode 1, (see Fig. S4 in the Supplemental Material [25]). The above self-similar scale-free scaling behaviors imply that the dynamics for determining the intermittent spatiotemporal excitations of coherent waves and large amplitude waves both follow their own self-similar rules over a wide range of scales.

Note that stochastic thermal kicks are the sources for disordered excitation and interruption. The strong mutual interaction generates spatiotemporal coherence. Their competition is the key for the above scale-free distributions. The scale-free size distribution of coherent clusters has also been observed in thermally driven Belousov-Zhabotinsky chemical reaction [9].

How are the instantaneous local amplitudes of different modes and local structural order correlated? Figure 3(c) depicts the correlation probability $C(\langle|\Psi_6|\rangle, A_m)$ of finding a local bond with instantaneous $\langle|\Psi_6|\rangle$ and A_m of mode m by subtracting off the uncorrelated probability, $P(\langle|\Psi_6|\rangle)P(A_m)$, from the joint probability, $P(\langle|\Psi_6|\rangle, A_m)$, i.e., $C(\langle|\Psi_6|\rangle, A_m) = P(\langle|\Psi_6|\rangle, A_m) - P(\langle|\Psi_6|\rangle)P(A_m)$. The two positive (yellow to brown) bumps in each panel show the regions with higher likelihood. Namely, the worse interlocking in the regions with poor structural order tends to allow the stronger thermally excited waves. The tendency is enhanced with increasing m. This can also be

manifested by comparing the low $\langle|\Psi_6|\rangle$ (red) patterns with the high A_m (yellow to red) patterns for each mode in Figs. 1(a) and 1(d), respectively. Note that larger amplitude low frequency transverse phonons in regions with poor structural order were also observed in glassy colloidal systems [18,19].

From the single particle motion view, D is a super-position of all wave modes. With gradually deteriorating local structural order, A_m of all modes tend to increase. However, a particle still exhibits cage rattling until the constructive superposition through phase synchronization of large amplitude slow modes, which generates hopping with large change of D and structural rearrangement. This also explains previous observations of hopping which tends to be preceded by increasing amplitudes of low pass filtered cage rattling and deteriorated structural order [13,16,26–30]. After hopping with a large change of D, the destructive interference of desynchronized waves resumes cage rattling.

In conclusion, through MCEEMD for decomposing directly visualized transverse particle motion into different-scale modes in the $(2+1)$D space-time space, we demonstrate that the thermally excited acoustic waves can be viewed as microscopic wave turbulence in the quasi-2D cold dusty plasma liquid at the individual level. In the xyt space, all modes exhibit intermittent excitation, propagation, scattering, and annihilation, in the form of clusters sharing similar generic behaviors. The rescaled sizes of the coherent phase clusters and the large amplitude clusters both exhibit self-similar scale-free power law distributions, akin to those in other extended nonlinear subexcitable systems driven by noise. The poor particle interlocking in the region with poor structural order is the key origin for supporting the stronger excitations of all modes, especially the slow modes. For individual particle motion, the synchronization of the drastic changing parts of the slow mode with increasing amplitude switches particle motion from cage rattling to cooperative hopping, followed by cage rattling with desynchronized phases of multiscale modes.

Our Letter sheds light on the generic multiscale coherent acoustic waveform behaviors and their correlations with local structural order and individual particle motions in other cold and glass-forming liquids. It also paves the way to unraveling multiscale coherent excitations of various microscopic wave turbulences not only in 3D cold and glass-forming liquids but also in different nonlinear extended systems at the atomic level.

[1] E. Falcon, C. Laroche, and S. Fauve, Phys. Rev. Lett. 98, 094503 (2007).

[2] H. Punzmann, M. G. Shats, and H. Xia, Phys. Rev. Lett. 103, 064502 (2009).

[3] A. S. Mikhailov and K. Showalter, Phys. Rep. 425, 79 (2006).

[4] D. Pierangeli, F. DiMei, G. DiDomenico, A. J. Agranat, C. Conti, and E. DelRe, Phys. Rev. Lett. 117, 183902 (2016).

[5] J. Pramanik, B. M. Veeresha, G. Prasad, A. Sen, and P. K. Kaw, Phys. Lett. A 312, 84 (2003).

[6] Y. Y. Tsai, M. C. Chang, and L. I, Phys. Rev. E 86, 045402 (R) (2012).

[7] P. C. Lin and L. I, Phys. Rev. Lett. 120, 135004 (2018).

[8] M. Farge, G. Pellegrino, and K. C. Schneider, Phys. Rev. Lett. 87, 054501 (2001).

[9] J. Wang, S. Kàdàr, P. Jung, and K. Showalter, Phys. Rev. Lett. 82, 855 (1999).

[10] F. H. Stillinger, J. Chem. Phys. 89, 6461 (1988).

[11] E. R. Weeks, J. C. Crocker, A. C. Levitt, A. Schofield, and D. A. Weitz, Science 287, 627 (2000).

[12] L. Assoud, F. Ebert, P. Keim, R. Messina, G. Maret, and H. Löwen, Phys. Rev. Lett. 102, 238301 (2009).

[13] R. Candelier, A. Widmer-Cooper, J. K. Kummerfeld, O. Dauchot, G. Biroli, P. Harrowell, and D. R. Reichman, Phys. Rev. Lett. 105, 135702 (2010).

[14] Y. J. Lai and L. I, Phys. Rev. Lett. 89, 155002 (2002).

[15] C. Yang, C. W. Io, and L. I, Phys. Rev. Lett. 109, 225003 (2012).

[16] Y. S. Su, Y. H. Liu, and L. I, Phys. Rev. Lett. 109, 195002 (2012).

[17] Y. S. Su, V. W. Io, and L. I, Phys. Rev. E 86, 016405 (2012).

[18] H. Shintani and H. Tanaka, Nat. Mater. 7, 870 (2008).

[19] R. Zargar, J. Russo, P. Schall, H. Tanaka, and D. Bonn, Europhys. Lett. 108, 38002 (2014).

[20] S. Nunomura, S. Zhdanov, D. Samsonov, and G. Morfill, Phys. Rev. Lett. 94, 045001 (2005).

[21] V. Nosenko, J. Goree, and A. Piel, Phys. Rev. Lett. 97, 115001 (2006).

[22] J. Goree, Z. Donkò, and P. Hartmann, Phys. Rev. E 85, 066401 (2012).

[23] A. Piel, D. Block, A. Melzer, M. Mulsow, J. Schablinski, A. Schella, F. Wieben, and J. Wilms, Eur. Phys. J. D 72, 80 (2018).

[24] L. Couëdel, V. Nosenko, M. Rubin-Zuzic, S. Zhdanov, Y. Elskens, T. Hall, and A. V. Ivlev, Phys. Rev. E 97, 043206 (2018).

[25] See Supplemental Material at http://link.aps.org/supplemental/10.1103/PhysRevLett.123.065002 for Videos 1 and 2. Video 1 shows the temporal evolutions of $D_m(x,y)/\overline{a_m}$ (first row), $A_m(x,y)$ (middle row), and $\phi_m(x,y)$ (third row) of modes 2, 4, and 6. Video 2 shows isophase ($\phi_m = 0.5\pi$) surfaces, color coded by normalized amplitude A_m, for modes 2, 4, and 6 in the xyt space, viewed at different angles.

[26] M. L. Manning and A. J. Liu, Phys. Rev. Lett. 107, 108302 (2011).

[27] K. Chen, M. L. Manning, P. J. Yunker, W. G. Ellenbroek, Z. Zhang, A. J. Liu, and A. G. Yodh, Phys. Rev. Lett. 107, 108301 (2011).

[28] A. Ghosh, V. Chikkadi, P. Schall, and D. Bonn, Phys. Rev. Lett. 107, 188303 (2011).

[29] A. Widmer-Cooper and P. Harrowell, Phys. Rev. Lett. **96,** 185701 (2006).

[30] L. Berthier and R. L. Jack, Phys. Rev. E **76,** 041509 (2007).

[31] C. A. Knapek, D. Samsonov, S. Zhdanov, U. Konopka, and G. E. Morfill, Phys. Rev. Lett. **98,** 015004 (2007).

[32] Y. Feng, J. Goree, and B. Liu, Phys. Rev. Lett. **100,** 205007 (2008).

[33] G. E. Morfill and A. V. Ivlev, Rev. Mod. Phys. **81,** 1353 (2009).

[34] N. P. Kryuchkov, E. V. Yakovlev, E. A. Gorbunov, L. Couëdel, A. M. Lipaev, and S. O. Yurchenko, Phys. Rev. Lett. **121,** 075003 (2018).

[35] C. Yang, W. Wang, and L. I, Phys. Rev. E **93,** 013202 (2016).

[36] J. Ashwin and A. Sen, Phys. Rev. Lett. **114,** 055002 (2015).

[37] M. Nambu, S. V. Vladimirov, and P. K. Shukla, Phys. Lett. A **203,** 40 (1995).

[38] N. E. Huang, Z. Shen, S. R. Long, M. C. Wu, H. H. Shih, Q. Zheng, N. C. Yen, C. C. Tung, and H. H. Liu, Proc. R. Soc. A **454,** 903 (1998).

[39] N. E. Huang, M. C. Wu, S. R. Long, S. S. P. Shen, W. Qu, P. Gloersen, and K. L. Fan, Proc. R. Soc. A **459,** 2317 (2003).

[40] N. E. Huang and Z. A. Wu, Rev. Geophys. **46,** RG2006 (2008).

[41] J. R. Yeh, J. S. Shieh, and N. E. Huang, Adv. Adapt. Data Anal. **02,** 135 (2010).

[42] To characterize the local structural order, the bond-orientational order (BOO) for particle j at $\mathbf{r}_j$ is measured as $\mathrm{BOO} = \Psi_6(\mathbf{r}_j) = (1/N_j) \sum_k \exp(i6\theta_{jk})$, where θ_{jk} is the angle of the bond from particle j to its nearest neighbor k, and N_j is the number of its nearest neighbors [43]. Local strain increases with decreasing $|\Psi_6|$. $|\Psi_6| = 1$ and < 0.4 for a perfect lattice site and a defect site with a nearest neighbor number deviating from 6, respectively [43].

[43] K. J. Strandburg, *Bond-Orientational Order in Condensed Matter Systems* (Springer, New York, 1992).

[44] M. A. Colominas, G. Schlotthauer, and M. Torres, Biomed. Signal Process. Control **14,** 19 (2014).

[45] For measuring $A_m(\mathbf{x}, t)$ and $\phi_m(\mathbf{x}, t)$, $A_m(t)$ and $\phi_m(t)$ from $D_m(t)$ for each adjacent particle pair in the xy plane at time t is first measured, and it is assigned as $A_m(t)$ and ϕ_m at the center position of each pair, respectively. Through triangulation-based cubic interpolation, $A_m(\mathbf{x}, t)$ and $\phi_m(\mathbf{x}, t)$ over the entire xy space can be obtained, and the isophase surfaces color coded by A_m in the xyt space can be plotted.